

Single-particle oxidation state and morphology of atmospheric iron aerosols

S. Takahama,¹ S. Gilardoni,^{1,2} and L. M. Russell¹

Received 10 January 2008; revised 17 July 2008; accepted 28 August 2008; published 18 November 2008.

[1] Sixty-three iron-containing particles from five field campaigns (PELTI, ACE-Asia, MILAGRO (urban location and aloft on NCAR C-130), INTEX-B) were characterized with scanning transmission X-ray microscopy and near-edge X-Ray absorption fine structure L-edge spectroscopy (NEXAFS-STXM). Particle sizes ranged from 0.2 to 4.5 μm and were found in many types of morphologies. Iron was found to exist in many different oxidation states with average Fe(II) to Fe(II) + Fe(III) ratios ranging from 0.0 to 0.73. Twenty-two inclusions and six agglomerations were found. For 29 particles, concurrent (spatially resolved) carbon K-edge absorption spectra were collected; X-ray images suggest that in some instances, there are clear phase barriers between iron and carbonaceous regions in agglomerations and irregular particles. Occurrences of Fe(II) fractions and organic functional group abundances among particles appeared primarily in two clusters, one group high in both values and the other low in both, though consistent correlations between the two variables within each particle were not observed. The reduced form of iron on particle surfaces was observed in 16 particles, possibly suggesting atmospheric processing. For this limited set of particles, neither inferred particle source nor surface processing was by itself a strong predictor of overall Fe(II) fraction, indicating that both are important for variables contributing to the observed Fe(II) fraction in the atmosphere. In addition, seven spherical particles from the ACE-Asia campaign showed an iron shell with an absence of iron toward the core. These particles have carbon spectra characteristics consistent with tarballs described by Posfai et al. (2004), Hand et al. (2005), and Tivanski et al. (2007), which were previously identified as homogeneous carbon spherules. In this work, NEXAFS-STXM has detected heterogeneities in iron distribution and redox state over individual particles, showing the existence of a variety of types of iron particles in the atmosphere. Such information can be useful in improving models of iron particles, including deposition and fate in seawater.

Citation: Takahama, S., S. Gilardoni, and L. M. Russell (2008), Single-particle oxidation state and morphology of atmospheric iron aerosols, *J. Geophys. Res.*, 113, D22202, doi:10.1029/2008JD009810.

1. Introduction

[2] Atmospheric aerosols contain sulfate, ammonium, nitrate, elemental carbon, organic compounds, trace metals, crustal elements, and water [Seinfeld and Pandis, 2006]. Iron is a trace metal that can be suspended from soil as dust or emitted by combustion processes, or emitted by other anthropogenic mechanisms (brake abrasion). In the atmosphere, iron in particles can be found as (oxy-)hydroxides or complexes with inorganic and organic ligands [Hoffmann et al., 1996]. Understanding the nature of iron particles is important in achieving insight into the processes by

which aerosol particles contribute to direct radiative forcing, cloud condensation activity, catalysis of sulfur oxidation, and destruction of organic ligands in aqueous droplets and phytoplankton productivity [Seinfeld and Pandis, 2006].

[3] Iron can undergo both oxidation and reduction reactions in atmospheric particles. In bioavailable form, iron is a micronutrient that can provide nutrients for phytoplankton that produce dimethyl sulfide (DMS), which can have a net cooling effect on the planet [Charlson et al., 1987]. As iron in the Fe(II) oxidation state is more water-soluble over a larger range of pH than Fe(III), Fe(II) is considered to be the more bioavailable form of iron. However, oxidation reactions can proceed very rapidly in solution; maintaining bioavailable concentrations of iron in the reduced form is dependent on stabilization by binding of ligands or photochemical reduction that convert Fe(III) back to Fe(II) [Coale et al., 1998]. Fung et al. [2000] suggests that mass of iron deposited from aerosols is 2 orders of magnitude larger than

¹Scripps Institution of Oceanography, University of California, San Diego, La Jolla, California, USA.

²Now at Climate Change Unit, Institute for Environment and Sustainability, JRC, Ispra, Italy.

Table 1. Summary of Samples Analyzed by STXM

Field Campaign	Study Period, Location	Minimum Altitude (m)	Maximum Altitude (m)	Number of Particles
PELTI	July 2000, Caribbean (NCAR C-130)	30	2300	2
ACE-Asia	April 2001, Sea of Japan (NCAR-C130)	30	3650	11
MILAGRO (Urban)	March 2006, Mexico City (urban ground site)	2200	2200	22
MILAGRO (Aircraft)	March 2006, Mexico mainland/ Yucatan peninsula (NCAR C-130)	2090	4340	17
INTEX-B	May 2006, U.S. West coast (NCAR C-130)	890	1920	17
Total				63

that contributed from upwelling and entrainment; much of the contribution comes from mineral dust aerosols that are largely insoluble upon emission [Mahowald *et al.*, 2005]. Jickells *et al.* [2005], Mahowald *et al.* [2005], Meskhidze and Nenes [2006], and Boyd *et al.* [2007] collectively present a review of iron's role in ocean fertilization, from the point of emission from dust sources to oxidation states measured in aerosols at different geographical locations. Understanding of iron particle oxidation state and factors contributing to its chemical transformations is desirable to reduce uncertainty in the geochemical cycling of iron.

[4] There are many ways in which iron and its oxidation state have been characterized by analytical techniques, which are described concisely by Majestic *et al.* [2007]. NEXAFS is a technique that can be used to study iron Fe(II) and Fe(III) composition nondestructively (requiring no sample extraction or derivatization). NEXAFS-STXM has a chemical sensitivity which makes it more suitable for studying atmospheric particulate matter than Mossbauer spectroscopy, the only other method which allows for direct probing of iron oxidations states. NEXAFS combined with STXM provides chemical and morphological information at the single-particle level. This spectromicroscopy technique provides insights into the mechanisms affecting iron distribution and oxidation in particles undergoing atmospheric processing.

[5] Majestic *et al.* [2007] used NEXAFS to estimate the reduced fraction of total iron in an ensemble of atmospheric aerosols. Dynes *et al.* [2006] used NEXAFS-STXM to map total iron and iron oxidation states in biological samples, an application that can be mirrored in atmospheric aerosols. In addition, Hopkins *et al.* [2007] and Takahama *et al.* [2007] have collectively examined a large set of carbon K-edge NEXAFS spectra of ambient particles and possible source materials, and observed particles with NEXAFS spectra resembling those of soot and other sources. Drawing upon this knowledge, we use overlapping carbon K-edge spectra when available to infer sources of the iron aerosols and what influence this may have on the iron oxidation state.

[6] This work has three objectives: (1) determine iron oxidation state through application of single-particle NEXAFS-STXM to the 63 atmospheric particles collected in different regions of the northern hemisphere, (2) determine if any relationships with organic functional groups can be detected, and (3) examine the heterogeneity in total iron distribution and oxidation states to gain insight into particle source emissions and reduction or oxidation processes in the atmosphere. In addition, we propose an estimate of the

relationship between redox state and pH domain of an aerosol, given its iron oxidation state.

2. Methods

[7] Methods for sample collection and physical/chemical interpretation of spectra are discussed in this section. Additional descriptions of techniques used for image analysis and registration, determination of particle geometry, and auxiliary calculations are described in Appendices A1 and A2.

2.1. Sample Collection and Analysis

[8] During five field campaigns, particles were collected on silicon nitride windows (Si_3N_4 ; Silson Ltd.) mounted on a rotating impactor (Streaker; PIXE International, Inc.). Aluminum or copper tubing was used to draw air into the impactor at 1 Lpm. Samples were frozen after collection; during storage and transportation until time of analysis (May 2006, February 2007, and July 2007). Sampled grids and windows were analyzed at the Advanced Light Source at Lawrence Berkeley National Laboratories (Berkeley, CA) Beamline 11.0.2 [Bluhm *et al.*, 2006] in a He-filled chamber maintained at 1 atm. The list of projects and number of particles examined from each is shown in Table 1. Transmission of photons at energy levels between 700 and 730 eV was measured over a minimum spatial resolution of 30 nm and converted to optical density.

[9] Regarding storage artifacts, Majestic *et al.* [2006] observed small or insignificant decrease in soluble fraction of Fe(II) in particulate matter over 6 months of storage at freezing temperatures. Samples from MILAGRO(U), MILAGRO(A) and INTEX-B were analyzed after 2–9 months of storage under dry, dark, and freezing conditions. Samples from PELTI and ACE-Asia were analyzed 5–6 years after collection. Samples rechecked after extended storage have shown no quantitative or qualitative differences. If changes in soluble Fe(II) fraction during storage conditions are indicative of the magnitude of changes in Fe(II) fractions, we should expect that the Fe(II) fractions are perhaps biased by a small amount with respect to their values at the time of collection.

2.2. Interpretation of Spectra

[10] Transmission recorded as a function of space and energy is converted to optical density [$A = -\log(I/I_0)$] using a clear section of the window as background (I_0). Iron L-edge spectra generally have two regions of absorbance, the first is approximately between 706 and 712 eV and denotes an electronic dipole transition between $2p_{3/2}$ and 3d orbitals,

also called the L_3 edge. The second region is located between 720 and 726 eV and denotes an electronic transition between $2p_{1/2}$ and $3d$ orbitals, and is also called the L_2 edge. At the L_3 edge there are generally two peaks for ferric iron compounds, one centered approximately around 708 eV and another at 710 eV; their exact location is complex-specific and their difference can be attributed at first approximation to the crystal field splitting energies $[\Delta E(e_g - t_{2g})]$, but these small shifts in location are obfuscated by orbital hybridization [Degroot *et al.*, 1989, 1990; Todd *et al.*, 2003a]. Ferrous iron compounds can exhibit only single peaks at both the L_3 and L_2 edge [Vanderlaan and Kirkman, 1992; Todd *et al.*, 2003b]. Interpretation is aided by the theoretical calculations of Vanderlaan and Kirkman [1992]. Carbon K-edge spectra are interpreted as discussed by Russell *et al.* [2002], Maria *et al.* [2004], and Takahama *et al.* [2007].

2.3. Fe(II) Fraction

[11] A fitting of normalized $FeCl_2$ and $FeCl_3$ reference spectra [Dynes *et al.*, 2006] to observed spectra is used to determine the relative contributions of Fe(II) and Fe(III). The fitting procedure is a linear model with nonnegativity constraints on the coefficients, similar to the “stackfit” routine described by Hitchcock *et al.* [2005]. If S is a vector representing the observed spectra, and $S_{ref,II}$ and $S_{ref,III}$ are reference spectra of Fe(II) and Fe(III) compounds, respectively,

$$S = \beta_0 + \beta_{II} S_{ref,II} + \beta_{III} S_{ref,III} + \epsilon. \quad (1)$$

In equation (1), β s are regression coefficients and ϵ is the disturbance or error. The term “Fe(II) fraction” (α in equation (2)) used hereafter will refer to the ratio of the Fe(II) coefficient to the sum of coefficient values of Fe(II) and Fe(III) obtained from

$$\alpha = \frac{\beta_{II}}{\beta_{II} + \beta_{III}}. \quad (2)$$

Majestic *et al.* [2007] estimate the contribution of Fe(II) to Fe(III) from ratios in t_{2g} and e_g -like peaks [Todd *et al.*, 2003a; Dynes *et al.*, 2006]. This method can yield similar results to the “stackfit” method, but the latter algorithm is more robust as it considers the full features of the spectra.

2.4. Estimation of Organic Functional Group Abundance

[12] Peaks of organic functional groups were fitted to the carbon K-edge absorption spectra. The fitting procedure is described by Lehmann *et al.* [2005], Hopkins *et al.* [2007], and Takahama *et al.* [2007]. The π^* bonds are modeled as Gaussian peaks with 1 eV full-width half maximums (FWHMs), σ^* as Gaussian peaks with ≤ 6 eV FWHMs, and K-edge as arc tangent function with 1 eV FWHMs.

2.5. Total Iron and Carbon

[13] Total carbon is estimated from the post-edge absorbance in carbon K-edge spectra (between 305 and 320 eV). For total iron, we use the total integral of the L_3 and L_2 areas after background (700 eV $\leq A < 704$ eV) subtraction.

2.6. Absorbance for a Spherical Particle

[14] For spherical particles (determined by visual classification), we compared the observed absorbance with that expected for a particle with spherical geometry. For radiation incident on a sphere, the dependence of absorption (A) on particle radius can be calculated by

$$A_i = \sigma t_i + \epsilon_i \quad \forall i \in Particle, \quad (3)$$

where

$$t_i = 2 R \sin(\cos^{-1}(r_i/R)), \quad (4)$$

where i denotes the index of a pixel belonging to the foreground (particle), R is the radius of the sphere calculated by the image analysis routine, ϵ_i is the error term, and σ is obtained from fitting the model to the observations of total iron and total carbon for $r_i > 0.6 R$, thus allowing us to compare our predictions of absorbance for the particle interior with the measurements.

2.7. Bulk/Surface Composition

[15] The spectra vector, S , from Equation (1) can also be decomposed into a bulk and surface contribution,

$$S = \gamma S^{(bulk)} + (1 - \gamma) S^{(surface)}. \quad (5)$$

The weighting variable, γ , is the optical thickness of the bulk relative to that of the entire particle. Each spectral component, $S^{(bulk)}$ and $S^{(surface)}$, can be decomposed separately into contributions from Fe(II) and Fe(III),

$$S^{(i)} = \beta_0^{(i)} + \beta_{II}^{(i)} S_{ref,II} + \beta_{III}^{(i)} S_{ref,III} + \epsilon^{(i)} \quad \forall i \in \{bulk, surface\}. \quad (6)$$

The Fe(II) fraction of the original spectra (equation (2)) can then be calculated from a weighted contribution of each of the coefficients (equation (7)), or, more concisely, as a weighted sum of the Fe(II) fraction in each of the components (equation (8)),

$$\alpha = \left(1 + \frac{\gamma \beta_{III}^{(bulk)} + (1 - \gamma) \beta_{III}^{(surface)}}{\gamma \beta_{II}^{(bulk)} + (1 - \gamma) \beta_{II}^{(surface)}} \right)^{-1} \quad (7)$$

$$= \gamma \alpha^{(bulk)} + (1 - \gamma) \alpha^{(surface)}, \quad (8)$$

where γ varies spatially over the particle; it can be expressed in terms of the distance function D (Appendix A2, equation (A1)),

$$\gamma(D) = \begin{cases} \rho^* \frac{\sin(\cos^{-1}(\rho^{*-1}(1-D/\rho)))}{\sin(\cos^{-1}(1-D/\rho))} & \text{if } D/\rho \leq 1 \\ 0 & \text{otherwise,} \end{cases} \quad (9)$$

where ρ is the radius of curvature of the iron surface. We approximate ρ as the radius of a circle containing the same 2-D projected area as the iron image. Here ρ^* is defined as the ratio of radius of curvature of the bulk component to the iron particle $(\rho^{(bulk)}/\rho)$.

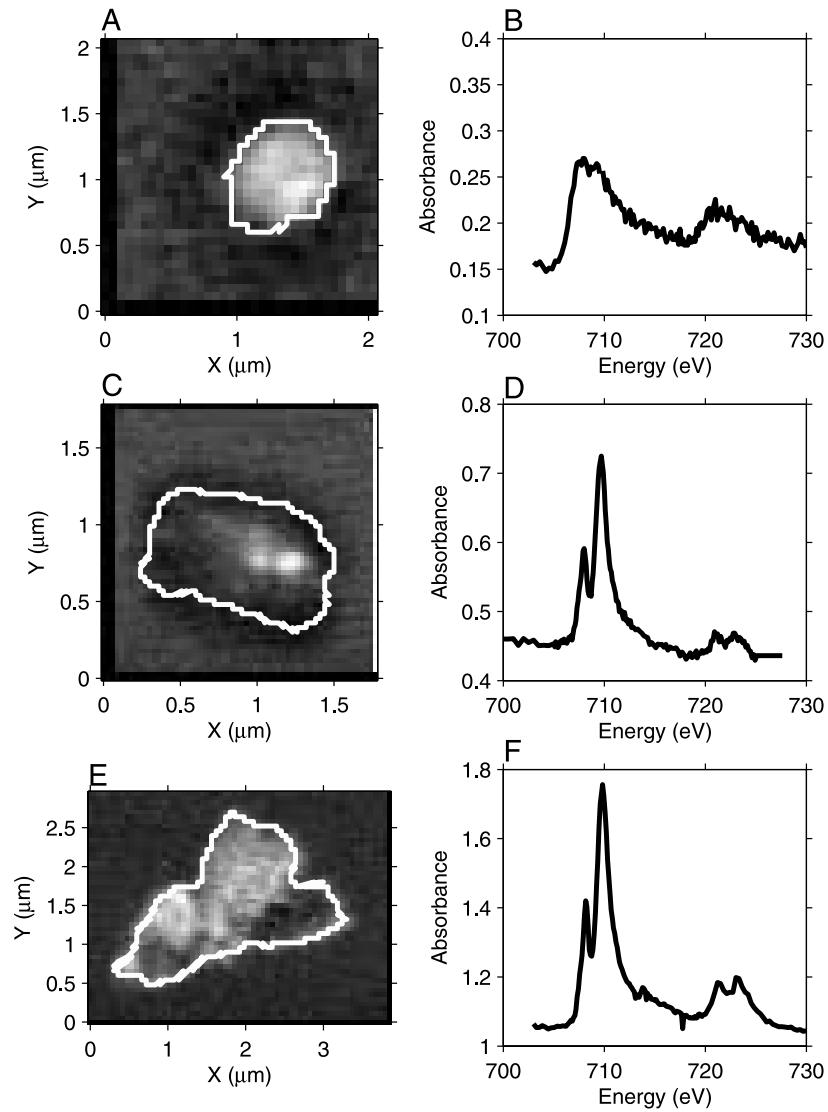


Figure 1. (a, c, e) Images of total iron intensity; whiter shading indicates higher iron content. Bright outlines are particle boundaries delineated by image analysis method. (b, d, f) Average spectra corresponding to iron regions from Figures 1a, 1c, and 1e, respectively.

[16] In essence, α is expressed as a nonlinear function in D . From a set of 27–125 initial conditions, we apply a nonlinear least squares [Bates and Watts, 1988] algorithm (nls function implemented in R [R Development Core Team, 2008]) to find the values of ρ^* , $\alpha^{(bulk)}$, $\alpha^{(surface)}$ which minimizes the sum-squared residuals (RSS) between equations (8) and (9) and observed values of Fe(II) fraction. The appropriateness of this model is tested against a base-case model; that is, $\alpha(D) = \alpha = \hat{\mu}_\alpha$, which is a single-parameter model that represents α only by its mean value with no dependence on D . The model that better represents the data is selected on the basis of the lower score according to the Bayesian Information Criterion (BIC), which considers the quality of the fit (RSS) but penalizes for lack of parsimony (i.e., requiring a larger number of free parameters). Approximating the curvature of the particle as a sphere is more valid near the particle surface and less toward the interior, but the surface points are necessarily given more weight as

the number of pixels on or near the surface are larger than the number of interior points for any particle.

3. Results and Discussion

[17] Sixty-three particles varying in size, shape, and Fe(II) fraction were studied. Figure 1 shows examples of a spherical particle (Figure 1a), an inclusion (Figure 1c), and an agglomeration (Figure 1e), and the spectra averaged over the domain in which iron is present (Figures 1b, 1d, and 1f, respectively). These particles ranged from 0.2 to 4.5 μm in diameter in many morphological configurations. There were 15 spherical particles and 48 irregular particles, as determined by visual inspection. The irregular particles include agglomerations (6) and particles in which iron exists as inclusions (22).

[18] The overall iron (II) fraction for each particle varied between 0 and 0.73. Within each particle, the interquartile range of Fe(II) fraction across pixels was on average below

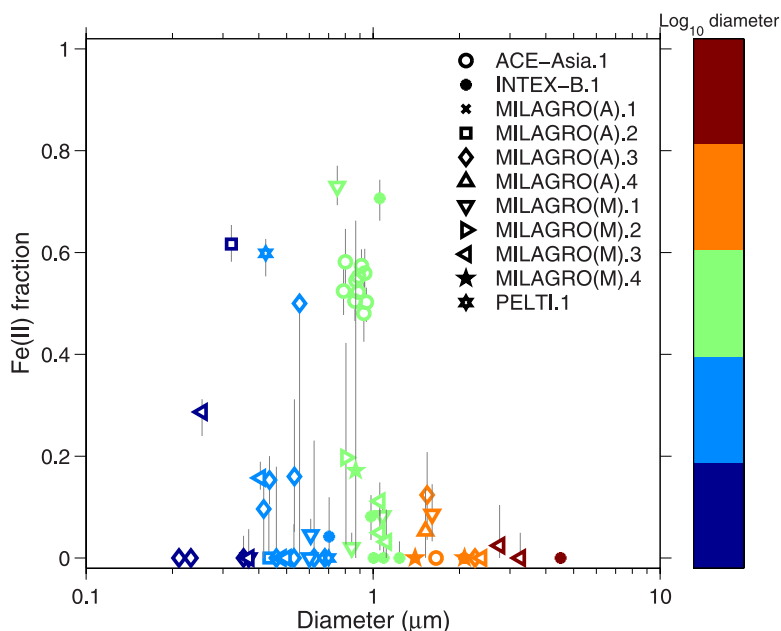


Figure 2. Fe(II) fraction and particle size (equivalent diameter of a projected sphere). Plotting symbols indicate location of overall Fe(II) fraction for a single particle; vertical bars span the interquartile range of Fe(II) fraction estimated for every pixel of the particle. Colors indicate particle size.

0.1, smaller than differences observed among particles. These ranges represent both variability and uncertainty introduced by the “noise” of the spectra and quality of the spectral fitting. Figure 2 shows the Fe(II) fraction (and its variability) and particle size for our samples, grouped by each sample window. For the sampling locations and sizes analyzed, significant variability in overall Fe(II) fraction is observed. The Fe(II) content also varied over different regions of the same particle, although on average the between-particle variations were greater. All 22 particles collected in Mexico City (MILAGRO(U)) had Fe(II) fractions less than 0.2; other STXM windows contained particles with a wider range of Fe(II) fractions. Bulk measurements of collocated filters analyzed by XRF indicated that the trace metal spectra for these Mexico City samples most closely resembled source profiles of refinery emissions, residential vegetative burning, and farm soil (Appendix A5).

[19] The observed range in single-particle Fe(II) fractions are consistent with ranges observed in measurements of particle ensembles by other groups (Figure 3). To place these measurements in context with respect to discussion of iron redox state and particle solubility, solubility fraction data are also shown for contrast in a separate row of panels. While Fe(II) is generally more soluble than Fe(III), iron redox state and solubility are not always related. Soluble iron includes some Fe(III) complexes and excludes some Fe(II) species, and direct comparisons of both Fe(II) and soluble Fe measurements show no consistent evidence of correlation. In marine aerosol, *Luo et al.* [2005] observed strong correlation between Fe(II) fraction and labile iron fraction, but *Zhu et al.* [1997] reported that large differences can exist between the dissolved fraction of total iron and that of Fe(II). *Majestic et al.* [2007] observed that for urban particulate matter, most of the soluble iron existed as Fe(II),

but in a controlled photochemical aging experiment of the ambient samples showed little relationship between changes in Fe(II) fraction and soluble fraction of iron aerosol from their initial values.

3.1. Iron, Carbon, and Fe(II) Distribution in Particles

[20] One of the advantages of STXM is the capability to detect heterogeneities within a single particle. Five types of heterogeneities (Figure 4) are discussed. These include inclusions, agglomerations, irregular particles, spherical particles with iron-deficient cores, and surface-reduced iron particles.

3.1.1. Inclusions

[21] Iron existing as inclusions, or multiple inclusions, was visible (e.g., Figure 1c). In these regions, the total iron intensity is significantly higher than the surrounding diffuse region (Figure 5a). If iron remains as an inclusion within insoluble material such as silicon or titanium, it may be inaccessible to reduction processes initiated by soluble compounds and may not become bioavailable in the ocean. In 90% of the inclusions, the Fe(II) fraction was less than 0.2 (Figure 5b), which is in the lower range of our observations. In 14 of the 22 particles, the Fe(II) fraction was statistically significantly higher (at the $\alpha = 0.95$ confidence level according to a two-sample *t*-test on the means) in the diffuse region surrounding the inclusion, indicating that some processing may have occurred, or that its origin is different from the rest of the particle. However, the detected difference in Fe(II) fraction was relatively small, less than 0.10 between the two regions in most (11) cases. To some extent this may be an underestimate if the inclusion is responsible for the difference in Fe(II) fraction; the reported difference is that between the diffuse region and column-integrated averages of Fe(II) fraction over the inclusion rather than the inclusion itself.

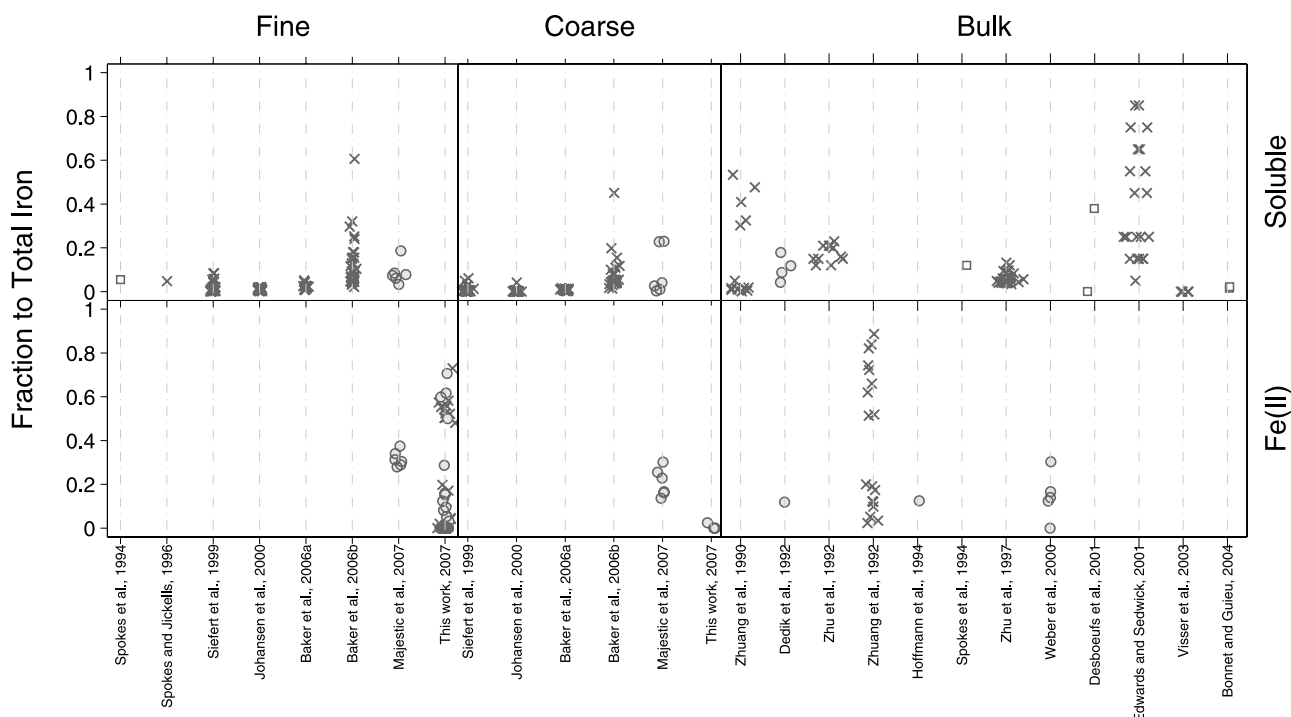


Figure 3. Fe(II) and soluble fractions of fine, coarse, and bulk iron samples. Cutoff between fine and coarse between 2 and 3 μm . Bulk includes both fine and coarse size fractions. Symbols indicate different degrees of atmospheric processing, determined by sampling location: remote (marine or arctic; x), continental (over developed continents; filled circle), source (particles sampled at source; square). References are: Zhuang *et al.* [1990]; Dedik *et al.* [1992]; Zhu *et al.* [1992]; Zhuang *et al.* [1992]; Hoffmann *et al.* [1994]; Spokes *et al.* [1994]; Spokes and Jickells [1996]; Zhu *et al.* [1997]; Siefert *et al.* [1999]; Johansen *et al.* [2000]; Weber *et al.* [2000]; Desboeufs *et al.* [2001]; Edwards and Sedwick [2001]; Visser *et al.* [2003]; Bonnet and Guieu [2004]; Baker *et al.* [2006a, 2006b]; Majestic *et al.* [2007].

3.1.2. Agglomerations and Irregular Particles

[22] For the six agglomerations identified, the area-equivalent particle diameters were greater than 0.8 μm with average Fe(II) fractions less than 0.2, indicating that iron in these agglomerations were found in a more oxidized form. In some regions of agglomerated and irregular particles, the iron and carbon existed mutually exclusively of each other (Figure 6). The Fe(II) fraction also varied systematically over different regions of particles. As Figure 7 shows, the spatial correlation, or gradient, in Fe(II) fraction across the particle suggests a structural or other nonrandom cause of variability. Agglomerations are reported in the literature [e.g., Post and Buseck, 1984; Pósfai *et al.*, 2003] and coagulation of constituent particles are included in models [Seinfeld and Pandis, 2006]. These spatially resolved chemical analyses shows that agglomeration processes combining organic and iron-containing particles do not necessarily produce homogeneous internal mixtures of organic and iron components.

3.1.3. Spherical Particles

[23] In a particular class of spherical particles, a distinct decrease in total iron content in the center of the particle relative to the outer regions was observed, suggesting the existence of an unidentified core material. Eight of these particles were observed: seven from ACE-Asia and one from MILAGRO(A), though the carbon content was below detection limit in the MILAGRO(A) particle. Figures 8a

and 8c show images of the same spherical particles at the carbon and iron edges, respectively, while Figures 8b and 8d show the total carbon and total iron content as a function of particle radius, respectively, along with a fitted line indicating the expected absorbance for a spherical particle. For both species, the fit for a sphere outside of the particle core is reasonable (some systematic deviation near the edges may result from particle impaction leading to the nonsphericity of the overall shape). The composition of the core of the aerosol particle is uncertain; correlations of residuals indicate that in some cases the decrease of iron may be compensated partially by increased carbon content. In six of the seven cases for which the carbon content was above detection limit, the correlation in residuals between the carbon and iron calculated from fitting equation (3) were significantly different from 0 at the $p = 0.05$ level. In one case, the correlation was 0.6, indicating a concurrent decrease in carbon; for four of the cases the correlation was negative and ranged between -0.1 and -0.4 . For the cases in which the correlation between carbon and iron residuals was significant, analysis of carbon K-edge spectra over different regions of the particle indicates that the core material is not different in carbon composition from the rest of the particle.

[24] The overall carbon NEXAFS spectra (Figure 9) of these particles resemble that of “tarballs” studied by NEXAFS [Tivanski *et al.*, 2007]. Most notably, concurrent presence

Description	Number	Conceptual Representation	Idealized Graphic
Inclusion.	22		
Particles with mutually exclusive regions of carbon and iron	13		
Agglomerated particles with spatially-correlated Fe(II) fraction.	6		
Core-shell particle. Spherical tarball particles from ACE-Asia campaign.	7		
Surface-reduced iron. Found in spherical and irregular morphologies.	16		

Figure 4. Categories of observed heterogeneities.

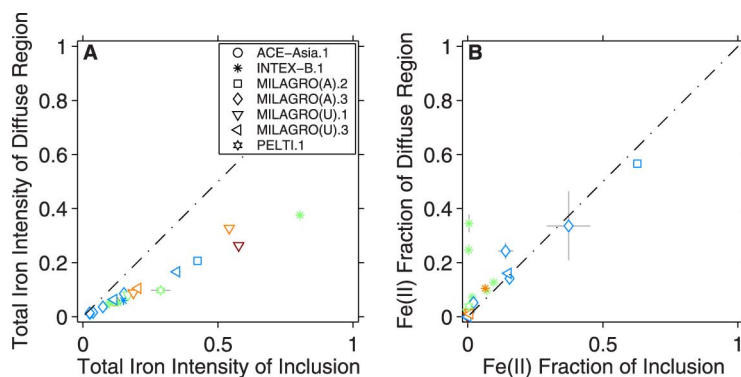


Figure 5. Comparison of (a) total iron intensity and (b) Fe(II) fraction in pixel regions of inclusions and diffuse region surrounding the inclusions. Symbol colors indicate particle size, as shown in Figure 2. Grey bars indicate standard errors in the estimated means of intensities and Fe(II) fractions.

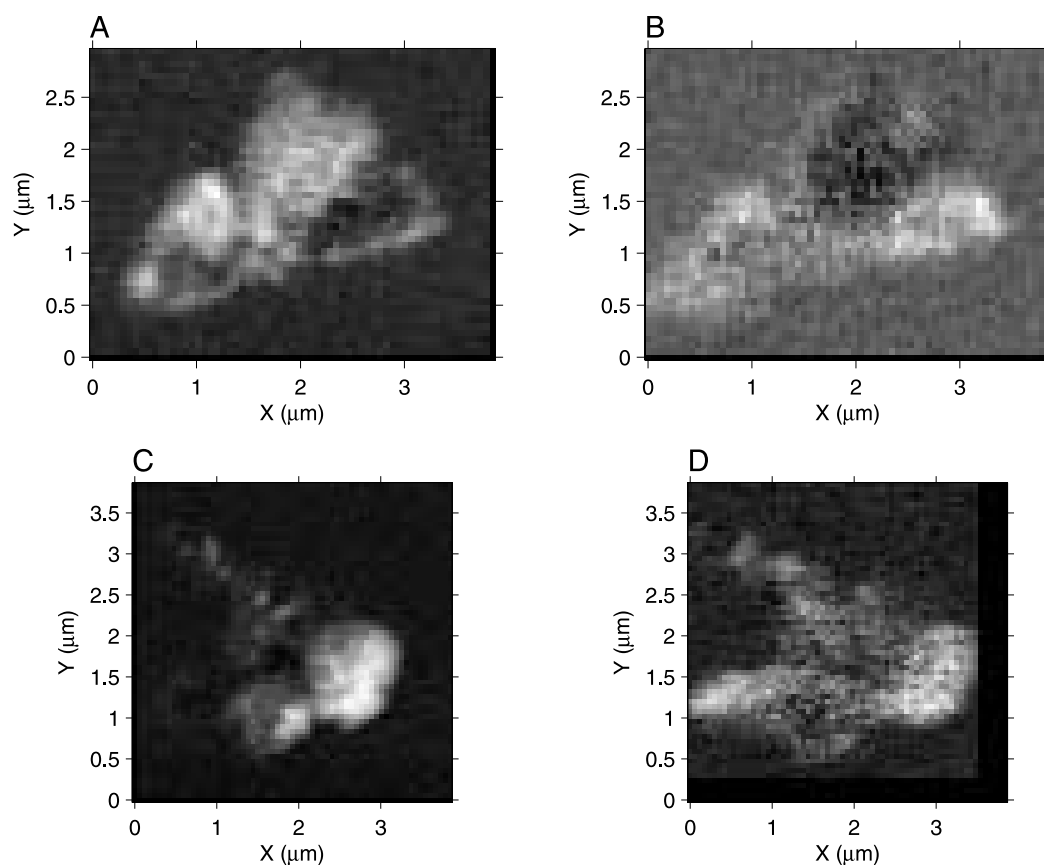


Figure 6. (a, c) Images of total carbon intensity and (b, d) corresponding images of total iron intensity for the same particle.

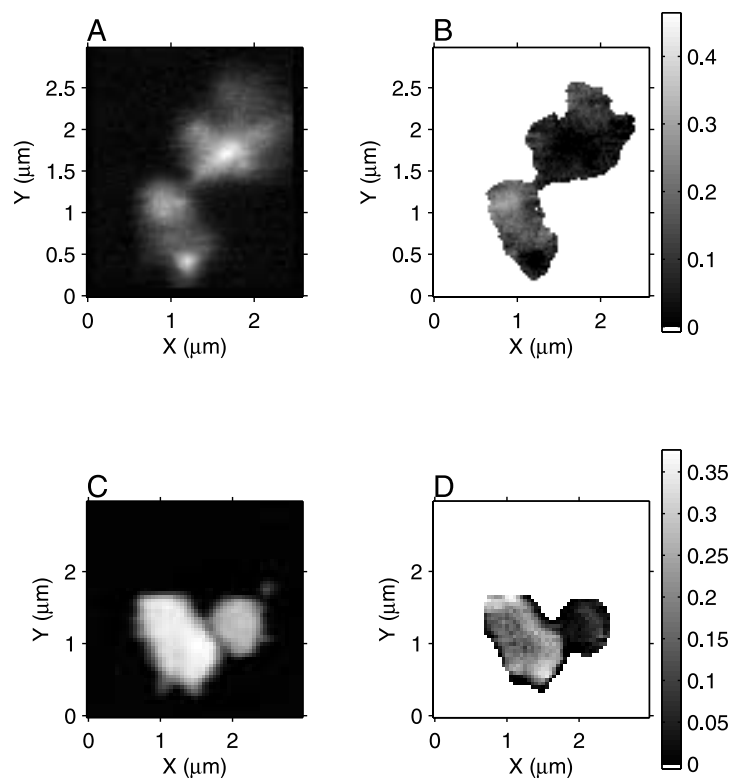


Figure 7. (a, c) Images of total iron intensity; white indicates higher iron content. (b, d) Corresponding Fe(II) fractions estimated by pixel.

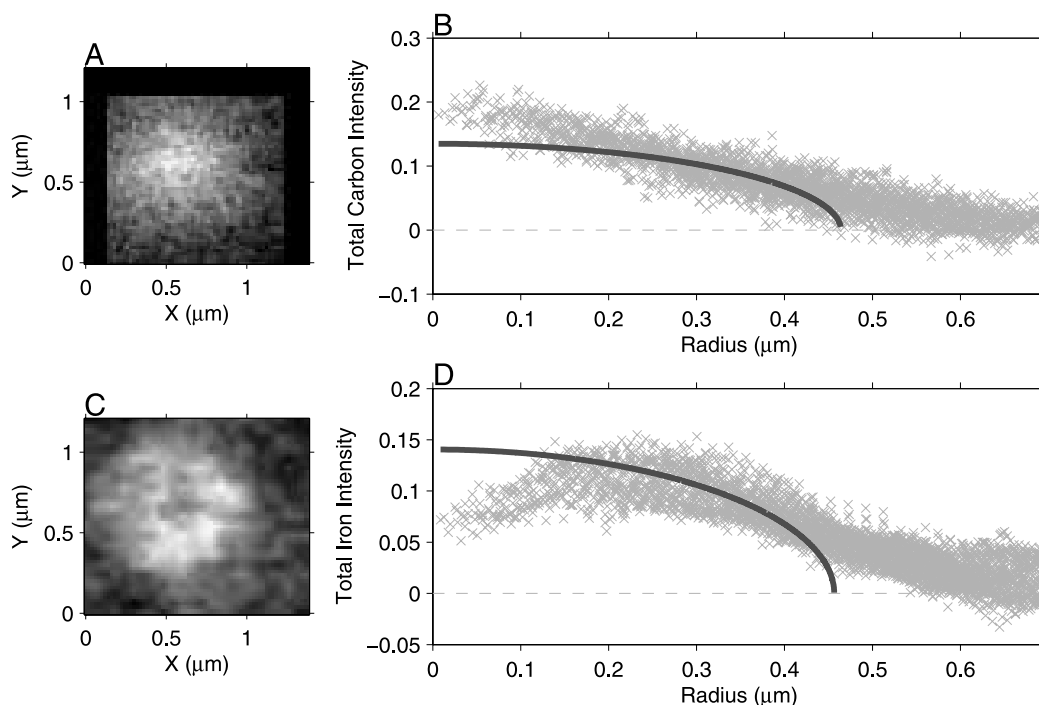


Figure 8. (a, c) Images of total carbon and total iron intensities, respectively. (b, d) Corresponding plots showing intensities of total carbon and total iron by pixel and radial distance from particle centroid. Dark lines are intensities expected for perfect spheres.

and relative magnitude of absorbance in the 285 and 289 eV regions (for C = C and C = OH bonds, respectively) indicate their similarity. A peak at 286 eV (for ketonic C = O bonds) is visible in the spectra by *Tivanski et al.* [2007] but is not visible in our spectra. A survey of over 600 particle spectra [Takahama *et al.*, 2007] illustrates that these differences are small with respect to the large variations observed among other spectra of atmospheric particles and source samples. *Pósfai et al.* [2004] suggest that tarballs originate in biomass burning events, and are comprised mainly of condensation products of low-volatility, hygroscopic organic carbon compounds that may undergo oligomerization. The Fe(II) fraction of these particles ranges on average from 0.48 to 0.58, which may be indicative of the oxidation states present upon

emission, or iron reduction may have resulted from aqueous reactions in the atmosphere. It is possible that an organic matrix prevents the iron from subsequent oxidation in the atmosphere. As *Pósfai et al.* [2004] and *Hand et al.* [2005] observes, there are other organic particles in the biomass plume that contain inorganic inclusions such as potassium, but tarballs contain little or very small amounts of potassium. The STXM images collected here confirm that tarballs do not contain a detectable level of potassium.

[25] Instances of these types of observed heterogeneities (agglomerations, irregular particles, inclusions, and iron-deficient cores) indicate that phase-separation (solid-solid, solid-liquid or aqueous-liquid) is energetically favored for dried particles. The effectiveness of iron as a catalyst for

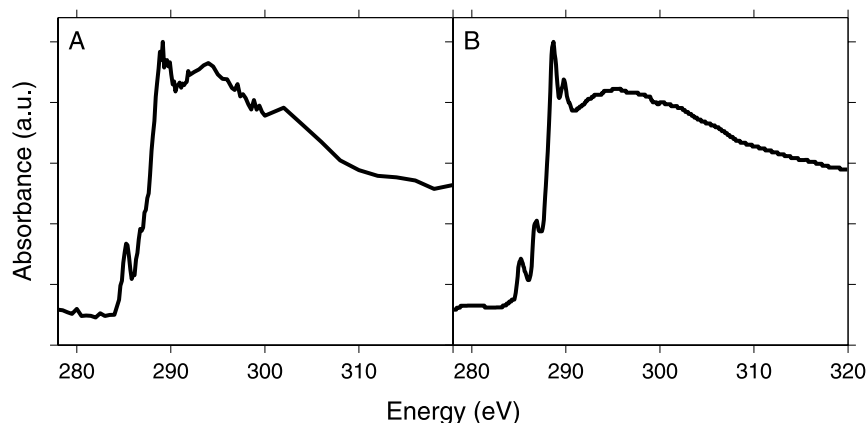


Figure 9. (a) Average spectra of seven spherical particles. (b) Spectra from biomass burning source reported by *Tivanski et al.* [2007].

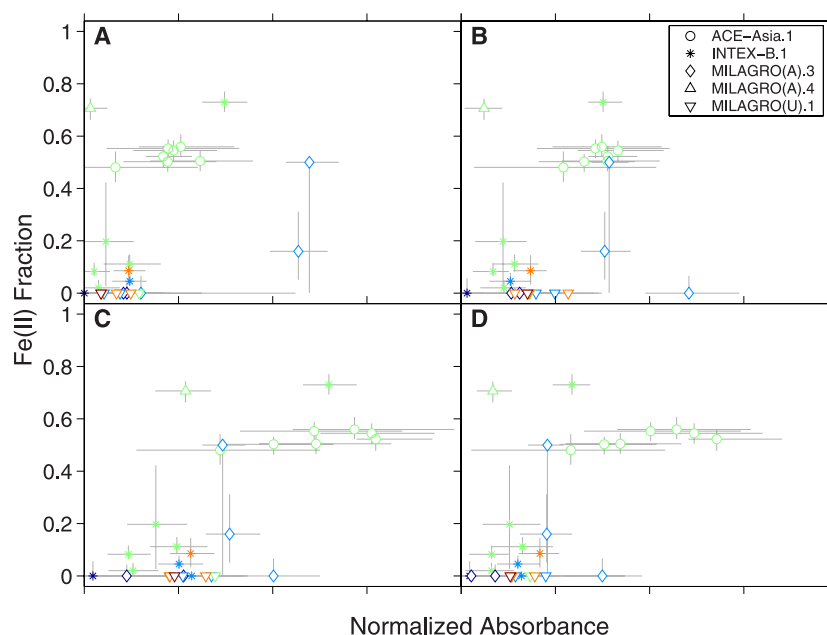


Figure 10. Scatterplot of Fe(II) fraction and organic functional groups: (a) ketonic carbonyl groups $[R(C=O)R]$; (b) alkyl groups $[R(C-H)_nR']$; (c) carboxylic carbonyl groups $[R(C=O)OH]$; and (d) alcohol and amide groups $[C-OH + CNH]$. Vertical grey bars indicate interquartile range of Fe(II) fraction calculated by pixel for each particle; horizontal grey bars indicate interquartile range of normalized functional group absorbances calculated by pixel for each particle. Symbol colors indicate particle size, as shown in Figure 2.

H_2O_2 production and subsequent oxidation of species such as SO_2 depends on the exposure of the iron to aqueous environments.

3.2. Fe(II) Fraction and Organic Functional Groups

[26] Concurrent iron and carbon spectra were available for 29 particles. The carbon spectra may provide information regarding the organic content of the particle (possible candidates for ligand formation), the degree of atmospheric processing, and possible sources. As Figure 10 shows, with a few exceptions, there are two main clusters in the absorbance-Fe(II)-fraction pairs (one domain containing particles high in both oxygenated organic functional-group content and Fe(II) fraction, and the other low in both functional group absorbance and Fe(II) fraction). One group is represented mainly by seven spherical particles from ACE-Asia exhibiting Fe(II) fractions between 0.5 and 0.7 with high oxygenated functional-group content (particularly carboxylic and alcohol/amide groups). The carbon K-edge spectra of these particles indicate that these particles may have originated in a biomass-burning event and are discussed in more detail in section 3.1.3.

[27] Organic ligands such as oxalic acid can reduce Fe(III) to Fe(II) [Suter *et al.*, 1988], and other organic compounds (e.g., tannic acid or other organic material of natural origin) can bind to Fe(II) to form oxidation-resistant complexes [Theis and Singer, 1974]. It is possible that such interactions are responsible for the concurrent observation of high functional group abundance and Fe(II) fraction in a group of particles. It is worth stating that these apparent “correlations” in Fe(II) fraction and organic functional groups observed do not necessarily imply causation (via

these atmospheric processing pathways) but can be the result of a number of variables, including the oxidation state of iron at time of emission. Luo *et al.* [2005] showed a weak correlation between oxalate concentrations and Fe(II) fraction for their bulk samples collected on several ocean cruises, indicating that the presence of reducing ligands do not necessarily result in reduced forms of iron.

[28] In contrast to the relationship observed across particles, correlations between organic functional group abundance and Fe(II) fraction by pixel within each particle ranged between -0.5 and 0.5 without a clear trend. This apparent randomness in correlation coefficients (absolute mean bias < 0.07), particularly in ACE-Asia samples, suggests that the quantity of organic functional groups may not be responsible for the variation in observed Fe(II) fraction. It is also possible that the variability in functional group abundance over a single particle is too small to observe its effect on Fe(II) fraction above the noise resulting from image processing and deconvolution of spectra (i.e., lack of statistical power). If the organic-ligand-induced reduction mechanism is indeed taking place, another explanation for the absence of consistent correlation is that these organic ligands are also destroyed in the process of oxidation [Zuo and Holgne, 1992].

3.3. Surface Processing of Fe(II)

[29] In a fraction of the particles, we observed a small increase in Fe(II) fraction near the particle surface (e.g., Figure 11). To quantify this effect, we converted the coordinates of each pixel from radial distance to distance from the surface (Appendix A2, Equation (A1)).

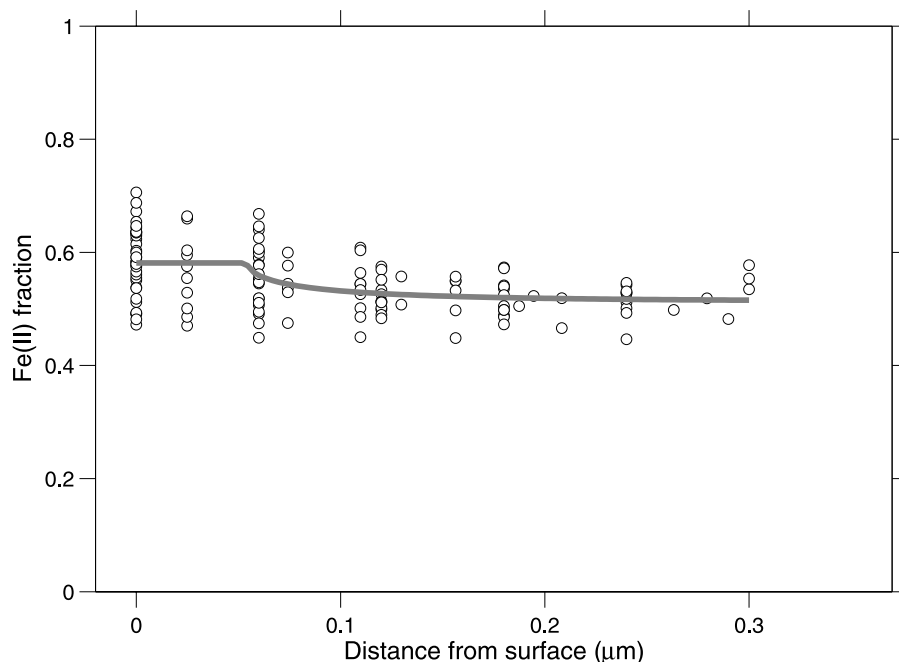


Figure 11. Fe(II) fraction as a function of distance from surface. Each point corresponds to Fe(II) fraction at a pixel. Grey line is model fit.

[30] For 16 particles, the bulk-surface model was scored favorably over the homogeneous model and had surface Fe(II)-fraction estimates higher than that in the bulk (p -values < 0.001 in all cases; Table 2 with additional notes in Appendix A3). These particles included two agglomerations, six inclusions, six irregular, and two spherical particles. The median thickness of the surface component was $0.02 \mu\text{m}$, with thicknesses less than $0.1 \mu\text{m}$ for 15 out of 16 particles. Differences in surface-bulk Fe(II) fractions ranged between 0.014 and 0.32 with a median difference of 0.06.

[31] The average Fe(II) fraction for the 16 core-shell-type particles ranged between 0 and 0.6, with all but one particle having an Fe(II) fraction below 0.2. With respect to all 63 particles analyzed (Figure 2), it is not clear that observation of reduced iron at the surface is indicative of a higher overall Fe(II) fraction.

[32] To further examine whether surface-related mechanisms could be responsible for the existence of reduced iron in atmospheric aerosols, we show the overall Fe(II) fractions together with estimated surface-area-to-volume ratio for each particle (Figure 12). There are many uncertainties introduced from estimating this ratio from a 2-D image and calculating a geometric surface area rather than a BET surface area value (Appendix A2), which captures surface microstructure characteristics. A considerable amount of scatter is visible in the data, indicating that the amount of reduced iron in aerosols are influenced by other variables than relative surface area.

[33] Atmospheric processing mechanisms that reduce iron (Appendix A1) may be facilitated by larger area-to-volume ratios of the aerosol particles, but the matrix composition of these particles may also play an important role in the final oxidation state that we observe. For the small number of particles analyzed here, the observed levels of reduced iron

appear to be affected by both initial state at emission (which is source dependent) and oxidant and radiation exposure (which is dependent on atmospheric processing). Since our particles were collected from different altitudes and environments (remote, rural, and urban), it is not surprising that neither source nor processing characteristics inferred from the data arise as the dominant factor governing iron aerosol oxidation state.

3.4. Redox Potential

[34] A simplified stability or predominance diagram [Pankow, 1991; Stumm and Morgan, 1996] for iron, with master variables selected to be pH and redox intensity (pe;

Table 2. Particle Characteristics and Fitted Parameters for Bulk-Surface Model^a

Particle Diameter (μm)	Fe(II) Fraction	ρ^*	$\alpha^{(bulk)}$	$\alpha^{(surface)}$
0.87	0.54	0.86	0.50	0.58
1.66	0.00	0.98	0.00	0.03
0.70	0.04	0.92	0.03	0.11
1.00	0.00	0.96	0.00	0.03
1.40	0.00	0.98	0.01	0.03
0.87	0.17	0.83	0.00	0.32
1.61	0.09	0.67	0.00	0.10
1.08	0.08	0.83	0.06	0.10
0.37	0.00	0.94	0.00	0.10
0.61	0.05	0.97	0.04	0.08
1.06	0.05	0.93	0.01	0.10
1.11	0.03	0.94	0.03	0.08
2.37	0.00	0.98	0.00	0.02
0.35	0.00	0.90	0.00	0.09
0.68	0.00	1.00	0.01	0.03
0.42	0.10	0.80	0.00	0.15

^aAll differences between estimated $\alpha^{(bulk)}$ and $\alpha^{(surface)}$ have p -values < 0.001 .

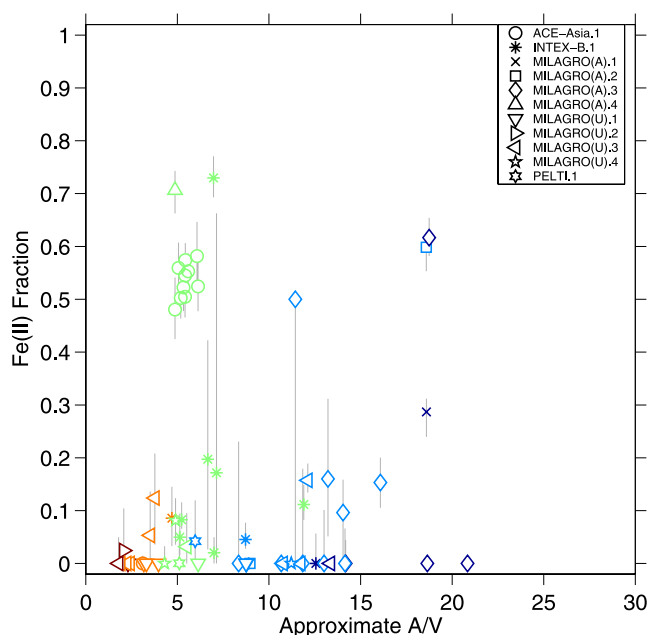


Figure 12. Overall Fe(II) fraction as a function of approximate surface-area-to-volume (A/V) ratio for particles, which is calculated as perimeter-to-area (P/A_c) from STXM images (equation (A2)). Vertical grey bars indicate interquartile range of Fe(II) fraction calculated by pixel for each particle. Symbol colors indicate particle size, as shown in Figure 2.

alternatively expressed as standard electrode potential or redox potential, E_H , scaled in volts), is shown in Figure 13. Measurements of pH and E_H in rainwater, snow, and cloud by Hoffmann *et al.* [1994] and Parazols *et al.* [2006] (symbols superposed in Figure 13) suggest that Fe^{2+} and varying proportions of $\text{Fe}(\text{OH})_2^+$ and $\text{Fe}(\text{OH})_3$ are favored under their observed conditions. Such information gives us useful information about the possible state of metal complexes in atmospheric water, dependent on the applicability of the assumption of system equilibrium. Past modeling studies on nitric acid partitioning indicate that chemical equilibrium of gas, solution, and solid can often be an acceptable approximation [e.g., Hildemann *et al.*, 1984; Takahama *et al.*, 2004]. In addition, since the region of pH- E_H space where mixtures of Fe(II) and Fe(III) can exist is small relative to their atmospherically relevant ranges, Fe(II) fractions estimated by NEXAFS may be able to provide a relationship from which one can infer the redox potential given the acidity (or vice versa).

[35] Many of the particles observed in this study are predominantly Fe(III). The mixed Fe(II)-Fe(III) character of some aerosol samples suggest that these particles are constrained to a limited pH-redox domain at chemical equilibrium. A possibility exists that mixed Fe(II)-Fe(III) values are a result of minerals containing both components or the coexistence of noninteracting solid phases of Fe(II) and Fe(III), but our spectra do not indicate such clear transitions within these particles. The uncertainty in our estimated value of Fe(II) fraction is large, but any mixed-character spectra indicating an Fe(II) fraction value between 0 and 1 will provide a useful basis for constraining either the pH or redox potential.

[36] While the majority of the diagram (Figure 13) indicates iron in the +2 or +3 oxidation states (Fe(II) fraction = 0 or 1), there is a small region that applies to a mixed-state sample. If observed values of Fe(II) fraction lie within this region, we can derive a relationship to estimate E_H from an additional estimate of pH. Figure 13 was created with consideration for a system containing only free iron and iron hydroxides, neglecting other inorganic ligands, organic ligands, and activity coefficients. The stability diagram can be modified to accommodate additional ligands and capture inherent nonidealities (Appendix A4), provided that the required information is available. If such variables are considered, Figure 13 and its variants can be used to investigate more realistic systems and possibly provide spatially resolved pH-redox information over a single particle.

4. Conclusions

[37] Sixty-three iron-containing particles from five field campaigns were studied with STXM and NEXAFS L-edge spectroscopy. Particle sizes ranged from 0.2 to 4.5 μm and were found in many types of morphologies. Iron was found to exist in many different Fe(II) fractions (averages ranging from 0.0 to 0.73). Twenty-two inclusions and six agglomerations were found, and images suggest that in some instances there are energy barriers to mixing of iron and carbon in agglomerations and other irregular particles. Seven spherical particles from the ACE-Asia campaign showed decrease of iron near the core. These particles are believed to be tarballs described by Pósfai *et al.* [2004], Hand *et al.* [2005] and Tivanski *et al.* [2007]. Decreases in iron content were accompanied by slight increases in carbon

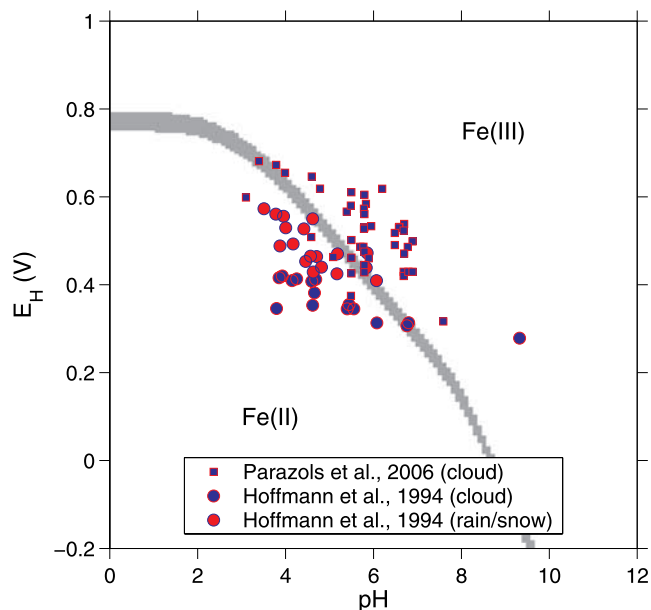


Figure 13. Predominance diagram. Shaded areas indicate Fe(II) fractions between 0.4 and 0.7. “Fe(II)” denotes region where Fe(II) fraction ~ 1 ; “Fe(III)” denotes region where Fe(II) fraction ~ 0 . Superposed measurements of atmospheric aqueous samples from Hoffmann *et al.* [1994] and Parazols *et al.* [2006].

intensity in four cases but at the present time there is no definitive evidence for what the core material(s) may be.

[38] A number of analysis techniques for NEXAFS-STXM data were used to examine evidence of atmospheric processing or source characteristics to observed oxidation state. Correlations between Fe(II) fraction and organic functional group abundance within individual particles varied between -0.5 and 0.5 with no clear pattern, but some correlation was observed between overall values estimated for each particle. One group of particles with high Fe(II) fraction and oxygenated organic functional groups contributing to this correlation across particles were biomass burning aerosols from ACE-Asia. In general, however, particles classified into sources by their carbon K-edge spectra did not show segregation in Fe(II) fraction, indicating that this categorization is not correlated to Fe(II) fraction of aerosols sampled in the atmosphere.

[39] The variability in Fe(II) fraction was analyzed as a function of distance from the surface. In sixteen particles, a bulk-surface model with statistically significantly higher Fe(II) fractions in the outer shell was found to be an appropriate fit. Our findings of higher Fe(II) fractions near the surface than toward the interior is consistent with surface reduction mechanisms for iron. However, the estimated differences in oxidation states between the two regions were small (median difference of 0.06), and examination of Fe(II) fraction and area-to-volume ratio of each particle did not show a strong relationship. While heterogeneities that might be considered evidence of surface reduction were observed, this type of processing also does not appear to explain the overall Fe(II) fractions in the aerosols that we have analyzed.

[40] We explored the relationships between a number of different indicators for source emission characteristics and surface processing at the single-particle level; neither factor alone was sufficient in explaining our observed Fe(II) fractions. It is likely that both factors are important and necessary to consider for predicting oxidation states of iron particles in the atmosphere.

[41] In this work, we present a new method for measuring iron oxidation state in individual atmospheric particles. NEXAFS-STXM has been demonstrated to be an analysis technique sensitive enough to detect heterogeneities in iron distribution and redox state over individual particles. Many different physical and chemical morphologies were found in our small number of samples. The particle types characterized here cannot be extrapolated to all particles in the atmosphere, but their existence provides a lower bound on the variety of particles in the atmosphere that may be important for modeling oxidation and deposition of iron. The observed particle characteristics summarized here can be useful in improving models of iron particles at various stages in their atmospheric lifetimes, including their role in ocean fertilization upon deposition into seawater.

Appendix A

A1. Image Analysis

[42] Several procedures were applied sequentially to delineate the particle boundary (i.e., differentiate the particle from the background). Axis2000 [Hitchcock *et al.*, 2000] was used to spatially align the images and convert trans-

mission to optical density values. Absorbance maps (stored as a 3-D array for space and energy dimensions) are imported into Matlab where a 2-D median filter (medfilt2) was applied to “despeckle” an image. This image is then passed to a classification algorithm (graythresh) which selects two clusters on the criteria of minimized within-class sum-of-squares [Otsu, 1979], effectively producing an intensity threshold above which pixels are considered to be a part of the aerosol. After an image is grey-leveled to binary values, an image labeling algorithm (imlabel) was applied (with a specification for eight-connected graphs) to select the desired particle in the image. From this series of procedures, the particle and its boundary is clearly demarcated from the background.

[43] To compare carbon and iron characteristics on a single-particle level, images were interpolated to the highest resolution and registered using normalized cross correlation (upon which Axis2000’s stackalign subroutine is also based), with carbon image at 288 eV and iron image at 709 eV selected for determination of spatial alignment parameters.

A2. Particle Geometry

[44] The particle “centroid” is calculated as the intensity-weighted mean of pixels belonging to the particle. Radial distance of each pixel is the Euclidean distance from this center. The distance function D for each foreground pixel i (a pixel belonging to the particle) is calculated as

$$D(i) = \min \{d(i, j) | j \in \text{Background}\}, \quad (\text{A1})$$

where $d(i, j)$ is the Euclidean distance between pixels i and j . The value of the distance function can be interpreted as the distance of each pixel from the particle surface. The particle “diameter” is computed as diameter of a circle containing the same 2-D projected area as the particle image.

[45] While direct area to volume ratio calculations are not possible from 2-D images acquired by STXM, particle images correspond to their maximum cross section. If the perimeter (P) to projected area (A_c) ratio at this cross section is proportional to the geometrical surface area (A) to volume (V) ratio; that is,

$$\frac{A}{V} = \frac{\int P(z) dz}{\int A_c(z) dz} \propto \left(\frac{P}{A_c} \right) \Big|_z, \quad (\text{A2})$$

where z is the axis parallel to the incident radiation and z' is the value of z at which the projected cross section is maximum. A/V is identical to P/A_c when P/A_c is independent of z . Figure A1 shows calculated P/A and A/V ratios as functions of particle volume (for a perfect sphere), with actual P/A_c ratios calculated for our particles superimposed. The true P/A_c for our particles appears to follow the idealized trend for A/V , indicating the utility of P/A_c in approximating the exposed area available for surface reactions. Therefore, we expect that P/A_c can be used as a reasonable surrogate for A/V .

[46] Underwood *et al.* [2000] reports a ratio of BET surface area (S_{BET}) to surface area of a sphere of the same average radius for $\alpha - \text{Fe}_2\text{O}_3$ powder; the value is 1.0 . However, iron (III) oxide in its γ phase ($\gamma - \text{Fe}_2\text{O}_3$) has an

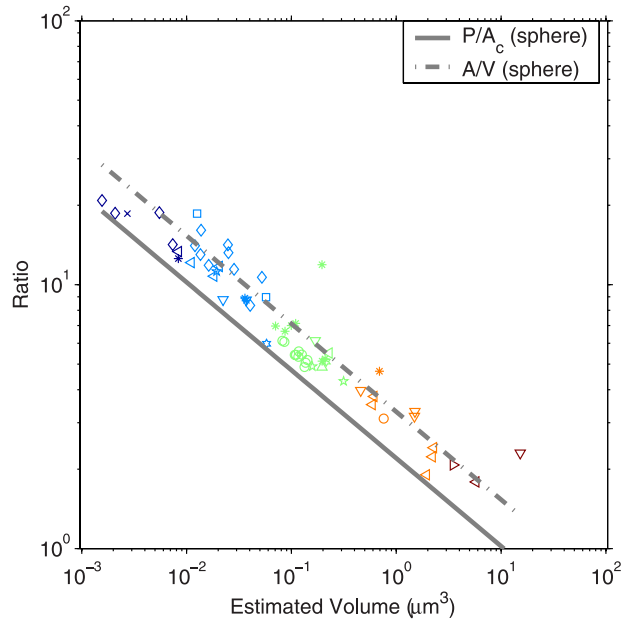


Figure A1. Perimeter-to-projected-area (P/A_c) ratio as a function of particle volume for real particles. Expected values of P/A_c and surface-area-to-volume (A/V) ratios for a sphere are superposed. Symbol colors indicate particle size, as shown in Figure 2.

S_{BET} an order of magnitude higher than in its α phase [Grassian, 2002; Fu et al., 2007].

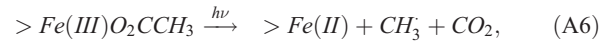
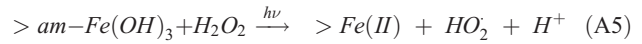
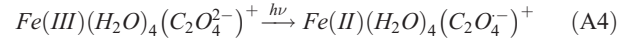
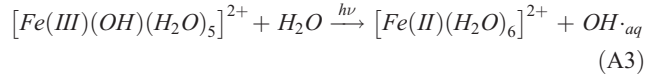
A3. Bulk-Surface Model

[47] If we assume that variations in Fe(II) fraction are caused by a structure that consists of a core and a shell, the bulk-surface model described in equations (8) and (9) can be fitted to observed values of Fe(II) fraction as a function of distance, D . The fit from this model was compared against that of a uniform or homogeneous model consisting of a single parameter (the mean value of Fe(II) fraction) using the Bayesian Information Criterion (BIC).

[48] It is possible that the physical constraints (nonnegativity) imposed on the fitting coefficients may lead to false positive detection of Fe(II) increases toward the surface. For instance, variability in Fe(II) fraction naturally increases toward the particle surface as the component of noise in the spectra of each pixel becomes large relative to the deterministic component (with decreasing optical thickness/iron content). Because the permissible values of the Fe(II) fraction is bounded by upper and lower bounds of one and zero, respectively, this would result in an asymmetric increase in variation and the mean Fe(II) fraction toward the particle surface for particles with low values of overall Fe(II) fraction. However, we observe increases in Fe(II) fractions for particles in which the lower bound constraint of zero is not active.

[49] Iron reduction at the particle surface is a surprising result, showing a trend opposite that reported for the common storage artifact of surface oxidation [Todd et al., 2003a]. Figure 11 shows an increase in Fe(II) fraction near the surface. Mechanisms for surface reduction of iron in the environment are well known. Reduction of iron can proceed

by several pathways [e.g., Zinder et al., 1986; Suter et al., 1988; Faust and Holgne, 1990; Zuo and Holgne, 1992; Zhuang et al., 1992; Pehkonen et al., 1993],



where “>” symbolizes a surface site. The first two reactions are bulk (volume) processes and are less likely to result in a nonuniform distribution of Fe(II) and Fe(III), unless the reactants (water or organic ligands) are distributed non-uniformly throughout the particle. The last two reactions suggest higher organic ligand or H_2O_2 concentrations localized to the surface can mobilize, and then reduce iron that is originally in insoluble form. Zhuang et al. [1992] and Mahowald et al. [2005] suggest that lifetime may be an important variable in estimating soluble fraction of Fe(II) following surface processing in the atmosphere.

A4. Calculation of Stability Diagram

[50] The Fe(II) fraction parameterized as a function of pH and pe [$\alpha(pH, pe)$] is

$$\alpha(pH, pe) = \frac{1}{1 + F(pe) \frac{G_{III}(pH)}{G_{II}(pH)}}, \quad (A7)$$

where

$$F(pe) = 10^{pe - \log K_{II,III}} \quad (A8)$$

$$G_{II}(pH) = 1 + \sum_i \frac{K_i}{(10^{-pH})^{\phi_i}} \quad (A9)$$

$$G_{III}(pH) = 1 + \sum_j \frac{K_j}{(10^{-pH})^{\phi_j}}. \quad (A10)$$

The values of Fe(II) fraction calculated by equation (A7) applies to iron in both the aqueous and solid phase. Precipitation of Fe(II) and Fe(III) solid species will occur when the solution is saturated with respect to Fe(II) or Fe(III) compounds in solution, respectively, but will not alter the diagram which shows the predominant oxidation state.

[51] Equations (A7)–(A10) can be extended to accommodate additional ligands and capture inherent nonidealities, provided that the required information are available. If estimated activity coefficients are incorporated into modified equilibrium constants (equilibrium constants cK_i are

estimated as $(\Pi_m \gamma_m^v K_i)$ and mass-law relationships of extra ligands with $[\text{Fe}^{2+}]$ are included in function L ,

$$G_{II}(\text{pH}, \lambda) = 1 + \sum_i \frac{^c K_i}{(10^{-\text{pH}})^{\phi_i}} + L(\lambda), \quad (\text{A11})$$

where λ is the concentration of additional ligands (organic and inorganic) available to complex with Fe^{2+} . A similar modification can be proposed for G_{III} . In this way the dependence of Fe(II) fraction can be varied parametrically with respect to pH , pe , and λ .

A5. Simultaneous Filter Measurements and Source Attribution

[52] During all field sampling campaigns in which samples for STXM analysis were collected, particles were concurrently collected on a collocated Teflon-filter sampler. These filters were analyzed by FTIR for organic functional groups [Gilardoni *et al.*, 2007] and X-ray fluorescence (XRF) by Chester LabNet (Tigard, OR) for elemental composition to aid in source identification.

[53] Trace-metal concentrations corresponding to each STXM sample were compared with source profiles in EPA's SPECIATE Version 4.0 database <http://www.epa.gov/ttn/chieff/software/speciate/> for "proximity" based on Euclidean distance. On the basis of availability of measured elements and quality of the data, 68 candidate sources from the database were selected. Sources most closely matching a number of our samples included farm soil, refinery, and residential wood or vegetative burning. STXM windows associated with the farm-soil source category contained only particles ($n = 14$) with Fe(II) fractions less than 0.2, while those associated with refinery emissions ($n = 45$) contained particles with a full range of Fe(II) fractions (0–0.73).

[54] As air masses sampled can contain a mixture of many different source emissions. Source attribution by bulk methods can at best provide information regarding the fractional contribution of different sources to a collection of particles, but cannot unambiguously identify the source of individual particles examined in our analysis. For instance, XRF element spectra corresponding to our ACE-Asia sample most closely matches that of refinery and gasoline exhaust spectra, but carbon K-edge spectra reveal that our particles are most likely derived from a biomass burning event.

[55] Particles belonging to the combustion class (all of which were collected on aircraft) as determined from carbon K-edge analysis exhibited a range of Fe(II) fractions: three particles below 0.2 and three above 0.4. In general, however, the source categories suggested from single-particle carbon K-edge classifications [Takahama *et al.*, 2007] were not effective predictors of Fe(II) fraction.

[56] **Acknowledgments.** The authors acknowledge grant support for this work from DOE (W/GEC05-010, MPC35TA-A5), NSF (ATM-0511772, ATM-0408501, ATM-0002035, ATM-0104707), and the James S. McDonnell Foundation. In addition, valuable assistance was provided in using ALS facilities and collecting NEXAFS spectra by M.K. Gilles and A. Tivanski, and also T. Tylliszczak, A.L.D. Kilcoyne, and P.S. Nico. J.R. Anderson, M.D. Rivera, R. Ramos, and the science and operation teams of the field experiments PELTI, ACE-Asia, MILAGRO, and INTEX-B also provided enormous assistance in sample collection. The authors also thank the reviewers for their valuable comments on the manuscript.

References

- Baker, A. R., T. D. Jickells, K. F. Biswas, K. Weston, and M. French (2006a), Nutrients in atmospheric aerosol particles along the Atlantic Meridional transect, *Deep Sea Res., Part II*, 53(14–16), 1706–1719.
- Baker, A. R., T. D. Jickells, M. Witt, and K. L. Linge (2006b), Trends in the solubility of iron, aluminium, manganese and phosphorus in aerosol collected over the Atlantic ocean, *Mar. Chem.*, 98(1), 43–58.
- Bates, D. M., and D. Watts (1988), *Nonlinear Regression Analysis and Its Applications*, John Wiley, Hoboken, N. J.
- Bluhm, H., et al. (2006), Soft X-ray microscopy and spectroscopy at the molecular environmental science beamline at the advanced light source, *J. Electron. Spectrosc. Relat. Phenom.*, 150, 86–104.
- Bonnet, S., and C. Guieu (2004), Dissolution of atmospheric iron in seawater, *Geophys. Res. Lett.*, 31, L03303, doi:10.1029/2003GL018423.
- Boyd, P. W., et al. (2007), Mesoscale iron enrichment experiments 1993–2005: Synthesis and future directions, *Science*, 315(5812), 612–617.
- Charlson, R. J., J. E. Lovelock, M. O. Andreae, and S. G. Warren (1987), Oceanic phytoplankton, atmospheric sulfur, cloud albedo and climate, *Nature*, 326(6114), 655–661.
- Coale, K. H., K. S. Johnson, S. E. Fitzwater, S. P. G. Blain, T. P. Stanton, and T. L. Coley (1998), IronEx-I, an in situ iron-enrichment experiment: Experimental design, implementation and results, *Deep Sea Res., Part II*, 45(6), 919–945.
- Dedik, A. N., P. Hoffmann, and J. Ensling (1992), Chemical characterization of iron in atmospheric aerosols, *Atmos. Environ., Part A*, 26(14), 2545–2548.
- Degroot, F. M. F., M. Grioni, J. C. Fuggle, J. Ghijsen, G. A. Sawatzky, and H. Petersen (1989), Oxygen 1s x-ray-absorption edges of transition-metal oxides, *Phys. Rev. B*, 40(8), 5715–5723.
- Degroot, F. M. F., J. C. Fuggle, B. T. Thole, and G. A. Sawatzky (1990), 2p x-ray absorption of 3d transition-metal compounds: An atomic multiplet description including the crystal field, *Phys. Rev. B*, 42(9), 5459–5468.
- Desboeufs, K. V., R. Losno, and J. L. Colin (2001), Factors influencing aerosol solubility during cloud processes, *Atmos. Environ.*, 35(20), 3529–3537.
- Dynes, J. J., T. Tylliszczak, T. Araki, J. R. Lawrence, G. D. W. Swerhone, G. G. Leppard, and A. P. Hitchcock (2006), Speciation and quantitative mapping of metal species in microbial biofilms using scanning transmission X-ray microscopy, *Environ. Sci. Technol.*, 40(5), 1556–1565.
- Edwards, R., and P. Sedwick (2001), Iron in East Antarctic snow: Implications for atmospheric iron deposition and algal production in Antarctic waters, *Geophys. Res. Lett.*, 28(20), 3907–3910.
- Faust, B. C., and J. Hoigne (1990), Photolysis of Fe(III) -hydroxy complexes as sources of OH radicals in clouds, fog and rain, *Atmos. Environ., Part A*, 24(1), 79–89.
- Fu, H. B., X. Wang, H. B. Wu, Y. Yin, and J. M. Chen (2007), Heterogeneous uptake and oxidation of SO_2 on iron oxides, *J. Phys. Chem. C*, 111(16), 6077–6085.
- Fung, I. Y., S. K. Meyn, I. Tegen, S. C. Doney, J. G. John, and J. K. B. Bishop (2000), Iron supply and demand in the upper ocean, *Global Biogeochem. Cycles*, 14(1), 281–295.
- Gilardoni, S., et al. (2007), Regional variation of organic functional groups in aerosol particles on four U. S. east coast platforms during the International Consortium for Atmospheric Research on Transport and Transformation 2004 campaign, *J. Geophys. Res.*, 112, D10S27, doi:10.1029/2006JD007737.
- Grassian, V. H. (2002), Chemical reactions of nitrogen oxides on the surface of oxide, carbonate, soot, and mineral dust particles: Implications for the chemical balance of the troposphere, *J. Phys. Chem. A*, 106(6), 860–877.
- Hand, J. L., et al. (2005), Optical, physical, and chemical properties of tar balls observed during the Yosemite Aerosol Characterization study, *J. Geophys. Res.*, 110, D21210, doi:10.1029/2004JD005728.
- Hildemann, L., A. Russell, and G. Cass (1984), Ammonia and nitric acid concentrations in equilibrium with atmospheric aerosols: Experiment vs theory, *Atmos. Environ.*, 18(9), 1737–1750.
- Hitchcock, A., et al. (2000), *aXis2000 Software Version 2.0c*, Hitchcock Group, McMaster University, Hamilton, Ont., Canada. (Available at <http://unicorn.mcmaster.ca/aXis2000.html>)
- Hitchcock, A. P., C. Morin, X. R. Zhang, T. Araki, J. Dynes, H. Stover, J. Brash, J. R. Lawrence, and G. G. Leppard (2005), Soft X-ray spectroscopy of biological and synthetic polymer systems, *J. Electron. Spectrosc. Relat. Phenom.*, 144, 259–269.
- Hoffmann, P., R. T. Sinne, A. N. Dedik, V. K. Karandashev, A. A. Malyshev, S. Weber, and H. M. Ortner (1994), Iron in atmospheric aqueous and particulate samples, *Fresenius J. Anal. Chem.*, 350(1–2), 34–37.
- Hoffmann, P., A. N. Dedik, J. Ensling, S. Weinbruch, S. Weber, T. Sinner, P. Gutlich, and H. M. Ortner (1996), Speciation of iron in atmospheric aerosol samples, *J. Aerosol Sci.*, 27(2), 325–337.

- Hopkins, R. J., A. V. Tivanski, B. D. Marten, and M. K. Gilles (2007), Chemical bonding and structure of black carbon reference materials and individual carbonaceous atmospheric aerosols, *J. Aerosol Sci.*, **38**(6), 573–591.
- Jickells, T. D., et al. (2005), Global iron connections between desert dust, ocean biogeochemistry, and climate, *Science*, **308**(5718), 67–71.
- Johansen, A. M., R. L. Siefert, and M. R. Hoffmann (2000), Chemical composition of aerosols collected over the tropical North Atlantic ocean, *J. Geophys. Res.*, **105**(D12), 15,277–15,312.
- Lehmann, J., B. Q. Liang, D. Solomon, M. Lerotic, F. Luizao, J. Kinyangi, T. Schäfer, S. Wirick, and C. Jacobsen (2005), Near-edge X-ray absorption fine structure (NEXAFS) spectroscopy for mapping nano-scale distribution of organic carbon forms in soil: Application to black carbon particles, *Global Biogeochem. Cycles*, **19**, GB1013, doi:10.1029/2004GB002435.
- Luo, C., N. M. Mahowald, N. Meskhidze, Y. Chen, R. L. Siefert, A. R. Baker, and A. M. Johansen (2005), Estimation of iron solubility from observations and a global aerosol model, *J. Geophys. Res.*, **110**, D23307, doi:10.1029/2005JD006059.
- Mahowald, N. M., A. R. Baker, G. Bergametti, N. Brooks, R. A. Duce, T. D. Jickells, N. Kubilay, J. M. Prospero, and I. Tegen (2005), Atmospheric global dust cycle and iron inputs to the ocean, *Global Biogeochem. Cycles*, **19**, GB4025, doi:10.1029/2004GB002402.
- Majestic, B. J., J. J. Schauer, M. M. Shafer, J. R. Turner, P. M. Fine, M. Singh, and C. Sioutas (2006), Development of a wet-chemical method for the speciation of iron in atmospheric aerosols, *Environ. Sci. Technol.*, **40**(7), 2346–2351.
- Majestic, B. J., J. J. Schauer, and M. M. Shafer (2007), Application of synchrotron radiation for measurement of iron red-ox speciation in atmospherically processed aerosols, *Atmos. Chem. Phys.*, **7**(10), 2475–2487.
- Maria, S. F., L. M. Russell, M. K. Gilles, and S. C. B. Myneni (2004), Organic aerosol growth mechanisms and their climate-forcing implications, *Science*, **306**(5703), 1921–1924.
- Meskhidze, N., and A. Nenes (2006), Phytoplankton and cloudiness in the Southern Ocean, *Science*, **314**(5804), 1419–1423.
- Otsu, N. (1979), Threshold selection method from gray-level histograms, *IEEE Trans. Syst. Man Cybernet.*, **9**(1), 62–66.
- Pankow, J. (1991), *Aquatic Chemistry Concepts*, CRC Press, Boca Raton, Fla.
- Parazols, M., A. Marinoni, P. Amato, O. Abida, P. Laj, and G. Mailhot (2006), Speciation and role of iron in cloud droplets at the puy de Dome station, *J. Atmos. Chem.*, **54**(3), 267–281.
- Pehkonen, S. O., R. Siefert, Y. Erel, S. Webb, and M. R. Hoffmann (1993), Photoreduction of iron oxyhydroxides in the presence of important atmospheric organic-compounds, *Environ. Sci. Technol.*, **27**(10), 2056–2062.
- Pósfai, M., R. Simonics, J. Li, P. V. Hobbs, and P. R. Buseck (2003), Individual aerosol particles from biomass burning in southern Africa: 1. Compositions and size distributions of carbonaceous particles, *J. Geophys. Res.*, **108**(D13), 8483, doi:10.1029/2002JD002291.
- Pósfai, M., A. Gelencsér, R. Simonics, K. Arató, J. Li, P. V. Hobbs, and P. R. Buseck (2004), Atmospheric tar balls: Particles from biomass and biofuel burning, *J. Geophys. Res.*, **109**, D06213, doi:10.1029/2003JD004169.
- Post, J. E., and P. R. Buseck (1984), Characterization of individual particles in the Phoenix urban aerosol using electron-beam instruments, *Environ. Sci. Technol.*, **18**(1), 35–42.
- R Development Core Team (2008), *R: A Language and Environment for Statistical Computing*, R Found. for Stat. Comput., Vienna.
- Russell, L. M., S. F. Maria, and S. C. B. Myneni (2002), Mapping organic coatings on atmospheric particles, *Geophys. Res. Lett.*, **29**(16), 1779, doi:10.1029/2002GL014874.
- Seinfeld, J. H., and S. N. Pandis (2006), *Atmospheric Chemistry and Physics*, 2nd ed., John Wiley, Hoboken, N. J.
- Siefert, R. L., A. M. Johansen, and M. R. Hoffmann (1999), Chemical characterization of ambient aerosol collected during the southwest monsoon and intermonsoon seasons over the Arabian Sea: Labile-Fe(II) and other trace metals, *J. Geophys. Res.*, **104**(D3), 3511–3526.
- Spokes, L. J., and T. D. Jickells (1996), Factors controlling the solubility of aerosol trace metals in the atmosphere and on mixing into seawater, *Aquat. Geochem.*, **1**, 355–374.
- Spokes, L. J., T. D. Jickells, and B. Lim (1994), Solubilization of aerosol trace-metals by cloud processing—A laboratory study, *Geochim. Cosmochim. Acta*, **58**(15), 3281–3287.
- Stumm, W., and J. J. Morgan (1996), *Aquatic Chemistry*, 3rd ed., John Wiley, Hoboken, N. J.
- Suter, D., C. Siefert, B. Sulzberger, and W. Stumm (1988), Catalytic dissolution of iron(III) (hydr)oxides by oxalic-acid in the presence of Fe(II), *Naturwissenschaften*, **75**(11), 571–573.
- Takahama, S., A. Wittig, D. Vayenas, C. Davidson, and S. Pandis (2004), Modeling the diurnal variation of nitrate during the Pittsburgh Air Quality Study, *J. Geophys. Res.*, **109**, D16S06, doi:10.1029/2003JD004149.
- Takahama, S., S. Gilardoni, L. M. Russell, and A. L. D. Kilcoyne (2007), Classification of multiple types of organic carbon composition in atmospheric particles by scanning transmission x-ray microscopy analysis, *Atmos. Environ.*, **41**(40), 9435–9451, doi:10.1016/j.atmosenv.2007.08.051.
- Theis, T. L., and P. C. Singer (1974), Complexation of iron(II) by organic-matter and its effect on iron(II) oxygenation, *Environ. Sci. Technol.*, **8**(6), 569–573.
- Tivanski, A. V., R. J. Hopkins, T. Tyliczszak, and M. K. Gilles (2007), Oxygenated interface on biomass burn tar balls determined by single particle scanning transmission X-ray microscopy, *J. Phys. Chem. A*, **111**(25), 5448–5458.
- Todd, E. C., D. M. Sherman, and J. A. Purton (2003a), Surface oxidation of pyrite under ambient atmospheric and aqueous (pH = 2 to 10) conditions: Electronic structure and mineralogy from X-ray absorption spectroscopy, *Geochim. Cosmochim. Acta*, **67**(5), 881–893.
- Todd, E. C., D. M. Sherman, and J. A. Purton (2003b), Surface oxidation of chalcopyrite (CuFeS₂) under ambient atmospheric and aqueous (pH 2–10) conditions: Cu, Fe L- and OK-edge X-ray spectroscopy, *Geochim. Cosmochim. Acta*, **67**(12), 2137–2146.
- Underwood, G. M., P. Li, C. R. Usher, and V. H. Grassian (2000), Determining accurate kinetic parameters of potentially important heterogeneous atmospheric reactions on solid particle surfaces with a Knudsen cell reactor, *J. Phys. Chem. A*, **104**(4), 819–829.
- Vanderlaan, G., and I. W. Kirkman (1992), The 2p absorption-spectra of 3d transition-metal compounds in tetrahedral and octahedral symmetry, *J. Phys. Condens. Matter*, **4**(16), 4189–4204.
- Visser, F., L. J. A. Gerringa, S. J. V. der Gaast, H. J. W. de Baar, and K. R. Timmermans (2003), The role of the reactivity and content of iron of aerosol dust on growth rates of two Antarctic diatom species, *J. Phycol.*, **39**(6), 1085–1094.
- Weber, S., P. Hoffmann, J. Ensling, A. N. Dedik, S. Weinbruch, G. Mieke, P. Gutlich, and H. M. Ortner (2000), Characterization of iron compounds from urban and rural aerosol sources, *J. Aerosol Sci.*, **31**(8), 987–997.
- Zhu, X. R., J. M. Prospero, F. J. Millero, D. L. Savoie, and G. W. Brass (1992), The solubility of ferric iron in marine mineral aerosol solutions at ambient relative humidities, *Mar. Chem.*, **38**(1–2), 91–107.
- Zhu, X. R., J. M. Prospero, and F. J. Millero (1997), Diel variability of soluble Fe(II) and soluble total Fe in North African dust in the trade winds at Barbados, *J. Geophys. Res.*, **102**(D17), 21,297–21,305.
- Zhuang, G., R. A. Duce, and D. R. Kester (1990), The dissolution of atmospheric iron in surface seawater of the open ocean, *J. Geophys. Res.*, **95**(C9), 16,207–16,216.
- Zhuang, G. S., Z. Yi, R. A. Duce, and P. R. Brown (1992), Link between iron and sulfur cycles suggested by detection of Fe(II) in remote marine aerosols, *Nature*, **355**(6360), 537–539.
- Zinder, B., G. Furrer, and W. Stumm (1986), The coordination chemistry of weathering. 2. Dissolution of Fe(III) oxides, *Geochim. Cosmochim. Acta*, **50**(9), 1861–1869.
- Zuo, Y. G., and J. Holgne (1992), Formation of hydrogen-peroxide and depletion of oxalic-acid in atmospheric water by photolysis of iron(III) oxalato complexes, *Environ. Sci. Technol.*, **26**(5), 1014–1022.

S. Gilardoni, Climate Change Unit, Institute for Environment and Sustainability, JRC, I-21020 Ispra, Italy.

L. M. Russell and S. Takahama, Scripps Institution of Oceanography, University of California, San Diego, 9500 Gilman Drive, Mail Code 0221, La Jolla, CA 92093-0221, USA. (lmrussell@ucsd.edu)